

Introducing Controlled Microporosity in Melt Electrowriting

Kilian Maria Arthur Mueller, Andreas Unterrainer, Diana Marcela Rojas-González, Elena De-Juan-Pardo, Marian Sebastian Willner, Julia Herzen, and Petra Mela*

Melt electrowriting (MEW) enables the electric field-assisted digital fabrication of precisely defined scaffold architectures of micron-sized fibers. However, charge accumulation and consequent disruption of the precoded pattern by fiber bridging prevents controlled printing at small interfiber distances. This, together with the periodical layer stacking characteristic for additive manufacturing, typically results in scaffolds with channel-like macroporosity, which need to be combined with other biofabrication techniques to achieve the desired microporosity for cellular infiltration. Therefore, a design strategy is devised to introduce controlled interconnected microporosity directly in MEW scaffolds by an algorithm that creates arrays of bridging-free parallel fibers, angularly shifted from layer to layer and starting at a random point to avoid periodical fiber stacking, and hence channel-like pores while defining micropores. This work hypothesizes that pore size can be controlled, decoupled from fiber diameter, and the mechanical properties, including anisotropy ratio, can be tuned. The authors demonstrate this while leveraging the platform for both flat and seamless tubular scaffolds and characterize them via micro-computed tomography and tensile loading. Lastly, successful cell ingrowth into the micropores and extracellular matrix formation are shown. This platform enables microporous scaffolds entirely via MEW that can be tailored to the architectural and mechanical requirements of the target tissues.

proliferation, differentiation, and ultimately the formation of new tissue.^[1–5]

Recently, the TE paradigm shifted from the classical cell-based/bioreactor approach to an in situ strategy with the aim to exploit the innate natural regenerative potential.^[6] In in situ TE, cell-free scaffolds are implanted to attract and harbor host cells directly at the site of implantation. Key advantages include lower regulatory burden for clinical translation and off-the-shelf availability.^[7,8] Cell-free scaffolds have to be carefully engineered to immediately withstand the in situ biomechanical loads,^[6] to closely match the mechanical characteristics of the targeted tissue to replace,^[9] and provide adequate porosity for cell infiltration.^[10]

There is a wide variety of technologies to fabricate porous scaffolds, for example, salt leaching,^[11] gas foaming,^[12] ice templating,^[13] and fiber forming techniques^[14] such as electrospinning. Solution electrospinning (SES) is one of the most used scaffold fabrication techniques. It generates a whipping jet which is collected on a target and results in a nonwoven fabric


of nano- to microfibers, where fiber diameter and pore size are inherently coupled.^[15]

Melt electrowriting (MEW) is a unique solvent-free fiber forming technique^[16] that can produce controlled fibers with a

1. Introduction

The concept of tissue engineering (TE) strongly relies on the availability of well-defined porous scaffolds that act as a micro-environment to support cellular colonization, migration,

K. M. A. Mueller, A. Unterrainer, D. M. Rojas-González, P. Mela
TUM School of Engineering and Design Department
of Mechanical Engineering Munich Institute of Biomedical Engineering
Technical University of Munich
Chair of Medical Materials and Implants
Boltzmannstrasse 15, 85748 Garching, Germany
E-mail: petra.mela@tum.de

 The ORCID identification number(s) for the author(s) of this article can be found under <https://doi.org/10.1002/admt.202201158>.

© 2023 The Authors. Advanced Materials Technologies published by Wiley-VCH GmbH. This is an open access article under the terms of the Creative Commons Attribution-NonCommercial License, which permits use, distribution and reproduction in any medium, provided the original work is properly cited and is not used for commercial purposes.

DOI: 10.1002/admt.202201158

E. De-Juan-Pardo
T3mPLATE
Harry Perkins Institute of Medical Research
QEII Medical Centre
and UWA Centre for Medical Research
The University of Western Australia
Perth, WA 6009, Australia

E. De-Juan-Pardo
School of Engineering
The University of Western Australia
Perth, WA 6009, Australia

M. S. Willner
Mitos GmbH
Lichtenbergstraße 8, 858748 Garching, Germany

J. Herzen
School of Natural Sciences
Department of Physics Munich Institute of Biomedical Engineering
Chair of Biomedical Physics
Technical University of Munich
James-Franck-Strasse 1, 85748 Garching, Germany

diameter in the range from sub-micron^[17] to tens of microns.^[18] In MEW a melted polymer jet is extruded from a spinneret and stabilized by a high-voltage electric field while it is travelling towards a collector.^[19] Collecting the fiber jet on a computer controlled translating plate or rotating mandrel,^[20–22] allows to accurately deposit the fiber in a direct writing mode and to form complex 3D scaffold architectures via additive manufacturing principles by stacking individual fiber layers.^[23] Depending on the application, a plethora of precisely defined pore morphologies has been investigated for MEW ranging from inter alia rectangular,^[24] triangular,^[25] hexagonal,^[26] sinusoidal^[27–29] to auxetic^[30] architectures.

Yet, functional MEW scaffolds fabricated to date are macroporous, featuring relatively large pores typically in the range of 100 μm and more.^[19] These scaffolds are often developed as 2.5D constructs with a defined macroporous pattern repeatedly stacked layer by layer. This is due to the fact that electrostatic forces between neighboring fibers limits the minimum inter-fiber distance.^[31] Below that limit, fiber bridging events occur, where fibers deviate from the deposition path, snap to an already deposited fiber, and thus introduce undesired defects in the final scaffold architecture. Studies suggest a minimum ratio of interfiber distance to fiber diameter of 12,^[32,33] while Kim et al. report ratios ranging from 4 to 12 strongly depending on fiber diameter and collector conditions.^[31] Also layer number plays an important role, as stacks of parallel fibers tend to bend toward neighboring ones with progressing height, hence increasing the interfiber distance is necessary for defect-free print results.^[31] This significantly restricts the potential use of MEW scaffolds for in situ TE applications. Therefore, macroporous MEW scaffolds have been complemented with other techniques providing the microporosity needed for efficient cellular infiltration as, for example, electrospinning^[34–37] or, as shown by our group, molding followed by salt-leaching/gas foaming.^[38]

With the aim of further expanding the versatility and potential of MEW, here we present a design strategy to achieve microporous scaffolds exclusively by MEW. The concept is based on superimposing angularly shifted sets of parallel fibers whose interdistance is larger than the bridging threshold value. By combining a partially randomized scaffold design via the direct writing capabilities of MEW 3D microporous scaffolds are obtained. This strategy allows to i) control pore morphology and size, ii) decouple fiber diameter and pore size, and iii) tune the mechanical properties from isotropic to highly anisotropic, for both flat and tubular scaffolds. We demonstrate the scaffolds' microporous ultrastructure by non-invasive micro computed tomography (microCT), verify their mechanical response in terms of Young's modulus and suture retention, as well as investigate their cell infiltration capabilities. Our design strategy broadens the scope of MEW toward scaffolds for in situ tissue engineering as well as other applications where such highly controllable fibrous structures are relevant, such as catalysis^[39] and energy storage.^[40,41]

2. Results and Discussion

2.1. Software Platform

To fabricate microporous scaffolds avoiding the detrimental effects of fiber bridging, we developed an algorithm based on

superimposing angularly shifted sets of parallel lines, whose interfiber distances (ID) do not fall below the minimum ID given to avoid fiber bridging. The algorithm generates the toolpaths for MEW as follows: first, a user defines the design space, an orientation vector (OV), and the interfiber distance (ID) (Figure 1A-i). The design space corresponds to the scaffold dimensions, the OV entails the angular directions of the parallel line sets with respect to the X axis of the design space, and the ID defines the distance between the parallel lines. Then, the first set of parallel lines oriented according to the first angle of the OV is generated starting from a random point in the design space (Figure 1A-ii). The distance between parallel lines (ID) can be either constant or randomly generated following a Gaussian distribution between a lower and upper limit. Unlike other additive manufacturing techniques, MEW continuously deposits a fiber jet that cannot be stopped and started again, as this would disrupt the Taylor cone. Therefore, the algorithm connects the parallel lines via tangent semicircles to provide smooth and uninterrupted toolpaths for MEW (Figure S1, Supporting Information). Such a set of connected parallel lines forms a layer. After this, the following layer consists of a set of parallel lines oriented according to the next value in the OV and are, therefore, angularly shifted with respect to the previous layer (Figure 1A-iii,iv and Video S1, Supporting Information). Consequently, the OV defines the number of sets of parallel lines and hence the number of layers that form a stack. To obtain a scaffold of a desired thickness, multiple stacks are printed, either by repeating the same stack (Figure 1A-v) or by newly generating each stack to further increase randomization. Although we schematically showed writing of a stack with a constant interfiber distance for the sake of simplicity in Figure 1A-ii, we implemented the randomly distributed ID option to avoid “flower-like” structures with large pores that might create voids likely too large to retain and host cells (Figure S2, Supporting Information). On the other hand, such voids in the thickness direction could hypothetically be foreseen as transport channels in scaffolds that exceed the diffusion limit of 150 to 200 μm for oxygen and nutrition.^[42,43] A description of the algorithm detailing the mathematical framework for the toolpath generation is provided in the Supporting Information.

We have developed an intuitive graphical user interface (GUI) in Matlab that, based on user defined input parameters, automatically outputs the motion commands in Gcode format to control the relative movement between print head and collector during MEW according to the described approach. A comprehensive overview of all pattern input options is presented in Figure S3, Supporting Information.

2.2. Decoupling Fiber Diameter and Pore Size Results in Controlled Microporosity

Our software platform allows to control size and shape of the pores by adjusting the interfiber distance and the OV (Figure 1B). Here, a smaller interfiber distance and angle increment will result in smaller pores. These two parameters can either be set independently of each other or in a synergetic fashion as exemplary shown for an isotropic stack of melt-electrowritten polycaprolactone (PCL) fibers in Figure 1B. An

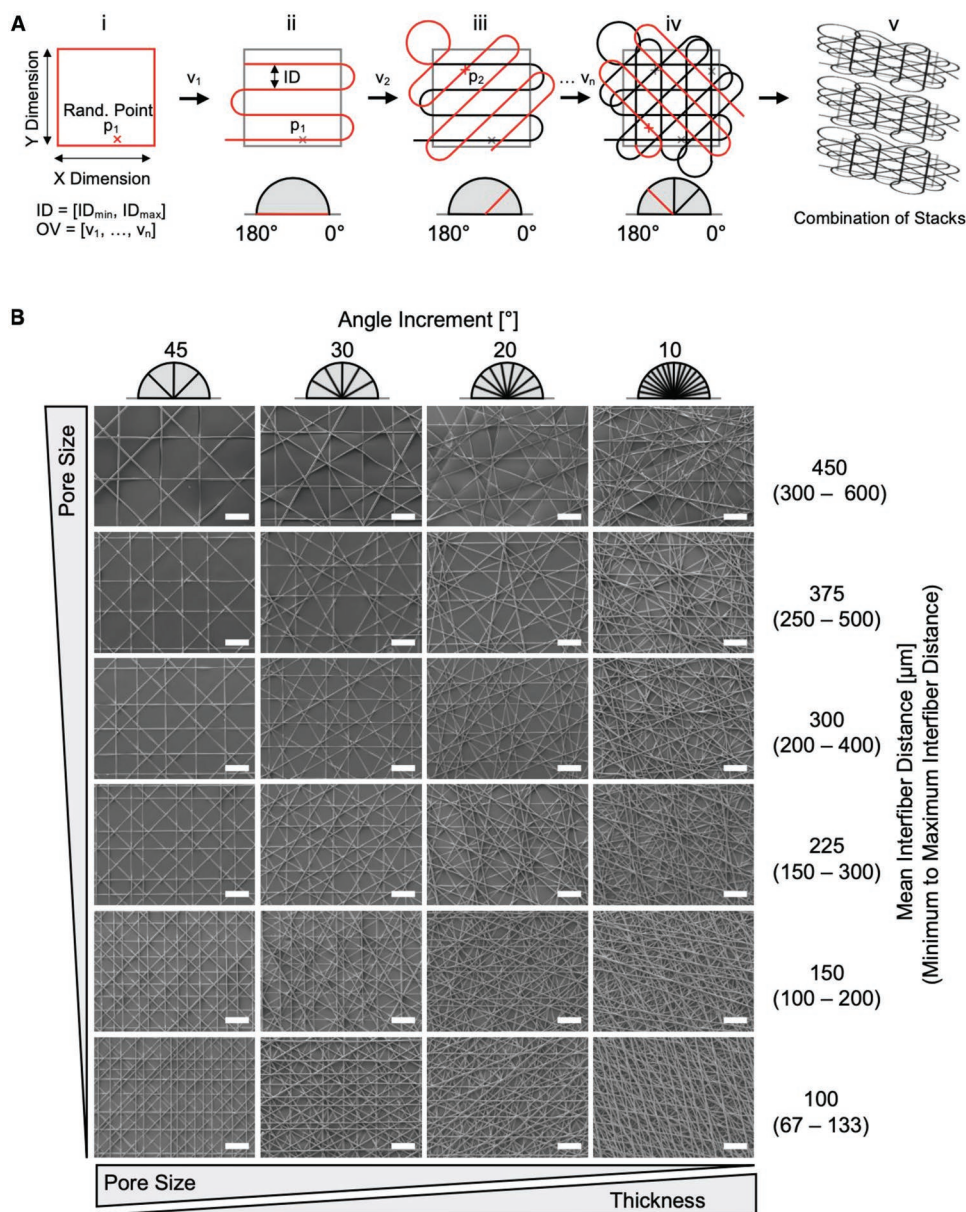


Figure 1. Design concept for the automated toolpath generation for scaffolds with highly tunable pore sizes. A-i) A design space is defined and starting from a random point p_1 , A-ii) a set of parallel lines is generated with interfiber distance ID and angle v_1 to form the first layer. A-iii) The second layer is generated starting again from a random point p_2 with interfiber distance ID and angle v_2 . A-iv) This procedure will be repeated for so many angles (n) as defined in the vector OV , in this way electrowriting a stack composed by n layers. A-v) By generating sequentially superimposed stacks, scaffolds of a desired thickness are obtained. The ID can be kept constant as in the process shown in (A) or can be randomly chosen within an upper and lower limit as done for the examples presented in (B). B) Scanning electron microscopy (SEM) images of melt-electrowritten stacks show that pore size can be tuned by interfiber distance and orientation vector independently. Smaller angle increments and/or a smaller interfiber distance will result in a smaller pore size and vice versa. The shown interfiber distances are each randomly distributed within the limits of mean $ID \pm 33\%$ (scale bars 200 μm).

increased number of entries in the OV — *ceteris paribus* — corresponds to an increased number of layers to be printed and thus to increased scaffold thickness. By repeatedly printing stacks, 3D scaffolds of desired thickness can easily be fabricated within the height limit inherent to MEW.^[44,45] The exceptional printing accuracy of MEW allows to translate the digitally coded scaffold architecture precisely into microporous scaffolds exhibiting a wide range of pore sizes, which can be optimally exploited for different TE applications.^[46–48] Typically, desirable

pore sizes span from a few tens to a few hundred microns ranging from roundish isotropic to elongated anisotropic morphologies.^[13,47] For tissue engineers this results in a strong need to have a fast method at hand that reproducibly fabricates scaffolds with a plethora of pore morphologies.

Next to pore size, fiber diameter plays a crucial role for cell attachment in the first place and the following tissue formation.^[49] However, in scaffolds manufactured by the widely used SES, pore size is directly related to fiber diameter, with

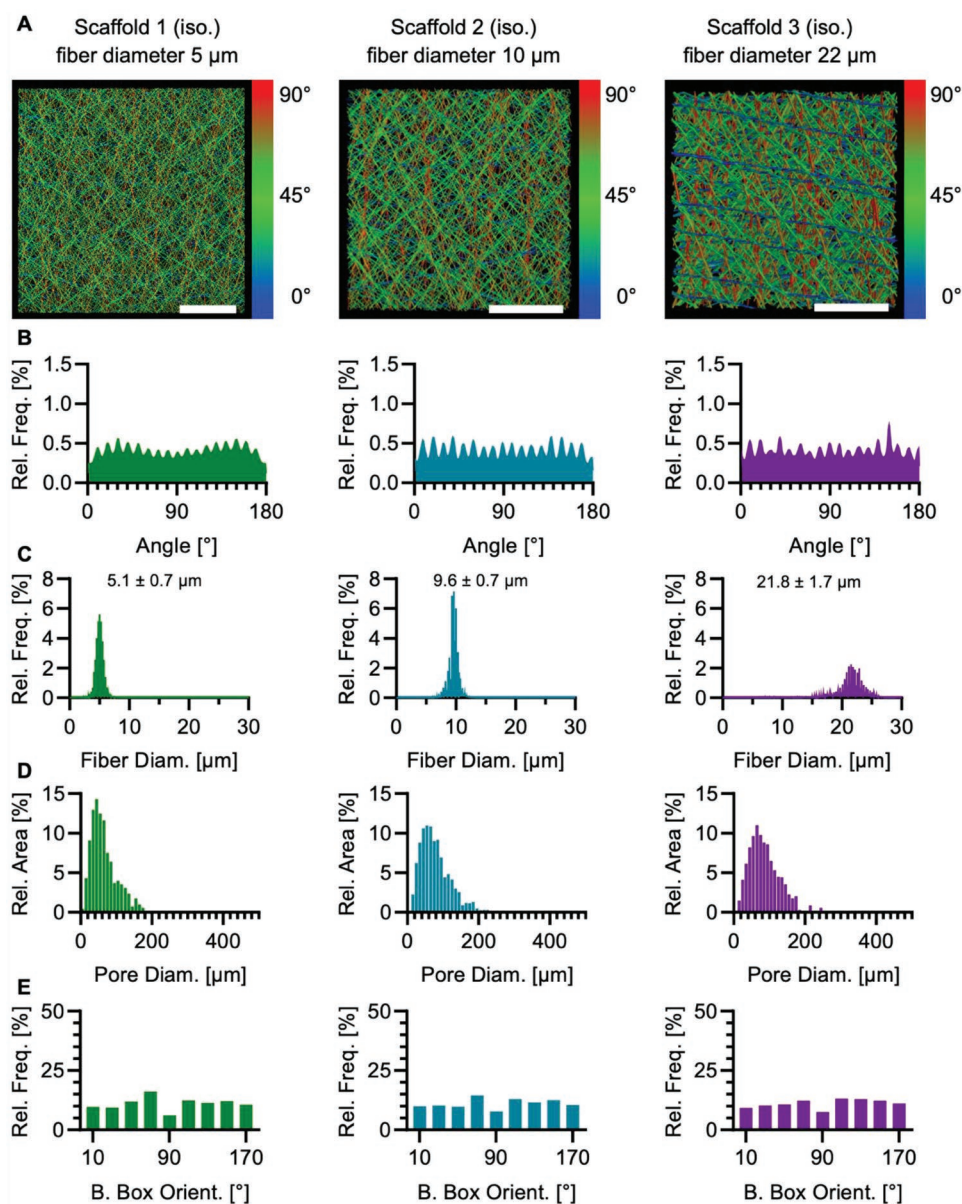


Figure 2. Control of fiber orientation, fiber diameter, and pore morphology in MEW scaffolds. A) Reconstructed microCT data of the same isotropic scaffold architecture fabricated with three different fiber diameters (scale bars 1 mm). Color coding represents the fiber orientations. Frequency distributions of the B) fiber orientations and C) fiber diameter. D) Frequency distributions of the pore diameters peaking at $\approx 45 \mu\text{m}$ independently of the fiber diameter. E) Oriented bounding boxes were fitted around the individual pores to derive a pore orientation. The pores of the scaffolds were evenly oriented from 0° to 180° .

smaller diameters resulting in denser matrixes with smaller pore sizes.^[15] This is due to the non-deterministic fiber deposition from a whipping jet in SES.^[15] On the contrary, we leverage the capability of MEW to produce fibers from the sub-micron range^[17] to several tens of microns^[18,19] and to precisely deposit them in a direct writing mode, to decouple fiber diameter from the resulting pore size.

To this end, we printed isotropic scaffolds with the same *OV*, *ID*, and number of stacks, but with different fibers diameters. Specifically: we chose an *OV* of 0° to 170° , in 10° intervals (i.e. 18 layers), randomized interfiber distance between 250 and $500 \mu\text{m}$ and four stacks. To verify the output of the software

platform, we analyzed the printed samples via non-invasive microCT (Figure 2). Renderings of the reconstructed microCT data reveal the fully interconnected fibrous network of the scaffolds. Fibers were color-coded according to their angular orientation, clearly showing the presence of angularly-shifted sets of lines (Figure 2A). Plots of the frequency of orientations highlight the capability of translating the digitally-coded fiber architecture into actual scaffolds via MEW (Figure 2B). Here, the peaks correspond to the predefined angles of the *OV* and were found from 0° to 170° in 10° intervals, exactly as coded by the software platform. Although all scaffolds had an equally designed architecture, they were fabricated using different fiber

diameter. The fibers diameters were determined as 5.1 ± 0.7 , 9.6 ± 0.7 , and $21.8 \pm 1.7 \mu\text{m}$ (Figure 2C). The different fiber diameters were achieved by tuning the air pressure at the print head, which drives the extrusion rate, as normally done in MEW.^[18] The scaffold with $21.8 \pm 1.7 \mu\text{m}$ fiber diameter showed minor signs of fiber pulsing,^[50] resulting in a larger standard deviation and broader fiber diameter distribution.

The increasing fiber diameter from scaffold 1 to scaffold 3 while keeping the same architecture, resulted in a higher fiber fraction volume and thus reduced porosity of 87 %, 85 %, and 83 %, respectively. Hence, tuning the fiber diameter is a valuable tool to effectively tailor porosity. Electrospun scaffolds typically feature a porosity of up to 80 %, ^[51] which, in the case of a successfully implanted in situ tissue-engineered heart valve based on an electrospun tubular scaffold, was 78 % to 81 %.^[10]

To determine the resulting pore size, we projected the 3D microCT data accounting for equivalent layer numbers, that is, a single stack, per scaffold into 2D representative images and analyzed them via bias-free algorithms (Figure S4, Supporting Information). This is analog to the widely established method to assess pore sizes of SES scaffolds via scanning electron microscopy (SEM) images.^[52–54] Hence, we report the projected dimensions of pore sizes in the *X/Y* plane (with the *Z* axis being the thickness direction), which are the critical structural features for cells that penetrate and invade a scaffold along its thickness direction.

We demonstrate that the isotropic scaffolds, indeed showed similar pore diameter distributions peaking at $\approx 45 \mu\text{m}$, although they were fabricated with different fiber diameters (5.1 ± 0.7 to $21.8 \pm 1.7 \mu\text{m}$, Figure 2D). In other words and in strong contrast to SES, we successfully decoupled fiber diameter from the resulting pore size. The pore size obtained here, is in the range of recommended values for tissue engineering of smooth muscle cells in arterial constructs^[55] or in porous elastin-like recombinamer hydrogels.^[56] However, the platform is not limited to this pore size but the scaffold design can rather be tuned via the *ID* and *OV* to result in far smaller or larger pore sizes according to specific needs. As exemplary shown for a single stack (Figure 1B), smaller angle increments in the *OV* and/or a smaller *ID* will result in a smaller pore size and vice versa, hence also for a 3D scaffold consisting of multiple stacks. This provides user controlled microporosity as long as the MEW process is performed in defect free direct writing mode, while it is at the discretion of the user to select the fiber diameter usually via the feeding air pressure. For $5 \mu\text{m}$ diameter fibers, we exemplary show an isotropic scaffold with an *ID* of $80 \mu\text{m}$ in Figure S5, Supporting Information, which results in a markedly reduced pore size as compared to the scaffolds shown in Figure 2. This design control is enabled by direct writing a stable fiber jet instead of randomly collecting a whipping turbulent fiber as known from electrospinning. Combining the direct writing capabilities of MEW according to computer-controlled pathways with its accurate control on fiber diameter enabled to decouple fiber diameter and pore size in fibrous scaffolds.

To highlight the isotropic scaffold design, we fitted oriented bounding boxes around the pores and found that they were evenly oriented from 0° to 170° (Figure 2E). Their orientation

resulted from the fibers that confine the pores and were oriented according to the isotropic *OV*.

Alternatively to the method presented here, one could apply travel speeds below the critical translation speed (CTS),^[57,58] which provokes the fiber jet to buckle and to form a coiling pattern that could be used as a microporous scaffold.^[59] However, this results in the loss of controlled fiber deposition now forming a non-woven mesh similar to SES, thus sacrificing the direct writing capabilities of MEW.

There is a large body of work reporting on optimal pore sizes and fiber diameters of fibrous scaffolds for specific target tissues,^[55,60,61] indicating also that different pore sizes within a scaffold may benefit its performance. Our software platform can serve this need by generating scaffold designs for MEW with nearly any pore size based on the user input data. By combining differently designed stacks, a pore size gradient over scaffold thickness can also be easily realized.

Analytical research on randomized fiber networks, such as electrospun fabrics, suggests that the distribution of pore size follows a Gamma-distribution,^[62–64] which is still true for our design concept based on controlled randomization (Figure 2D and Table S1, Supporting Information). A Gamma-distribution implies the coexistence of different pore sizes within the same scaffold, which has been suggested to benefit the overall performance of a scaffold in the sense that larger pores enable efficient infiltration while smaller pores enhance cell–cell communication and promote extracellular matrix formation.^[60,61]

Here, we introduce controlled randomization by accurately depositing microfibers according to algorithmically randomized and computer-controlled pathways. By changing the fiber paths layer by layer, as opposed to MEW scaffolds designed with constant patterns,^[19] we move away from 2.5D scaffold designs and, hence, we significantly expand the potential of melt-electrowritten scaffolds to host cells in scaffolds with a controlled microporosity.

2.3. Fiber Architecture Steers Ratio of Anisotropy

An *OV* entailing evenly distributed angles from 0° to 180° results in isotropic scaffolds (Figure 3A-i). However, the platform also enables the fabrication of anisotropic scaffolds, by simply restricting the boundary values of the *OV* (only angles greater than 0° and/or smaller than 180°).

The extent of this restriction tailors the level of anisotropy, of which the overall resulting fiber direction can be calculated as average: $(OV_{\min} + OV_{\max})/2$. Furthermore, we have the flexibility of choosing different *OV* resulting in the same average fiber direction, which allows to change the pore morphology from roundish to distinctly elongated. This aspect is shown in Figure 3A-ii,iii for scaffolds consisting of a single stack. For example, a scaffold with fiber orientations of 0° , 30° , 60° , and 90° (Figure 3A-ii), will result in an average fiber direction of 45° . The smaller the difference between OV_{\min} and OV_{\max} , the more pronounced the effect of anisotropy in terms of fiber architecture will be, without changing the average fiber direction. This can be appreciated in Figure 3A-iii for a scaffold with fiber orientations of 10° , 33.3° , 56.6° , and 80° , which is still characterized by an overall resulting fiber direction of 45° , but

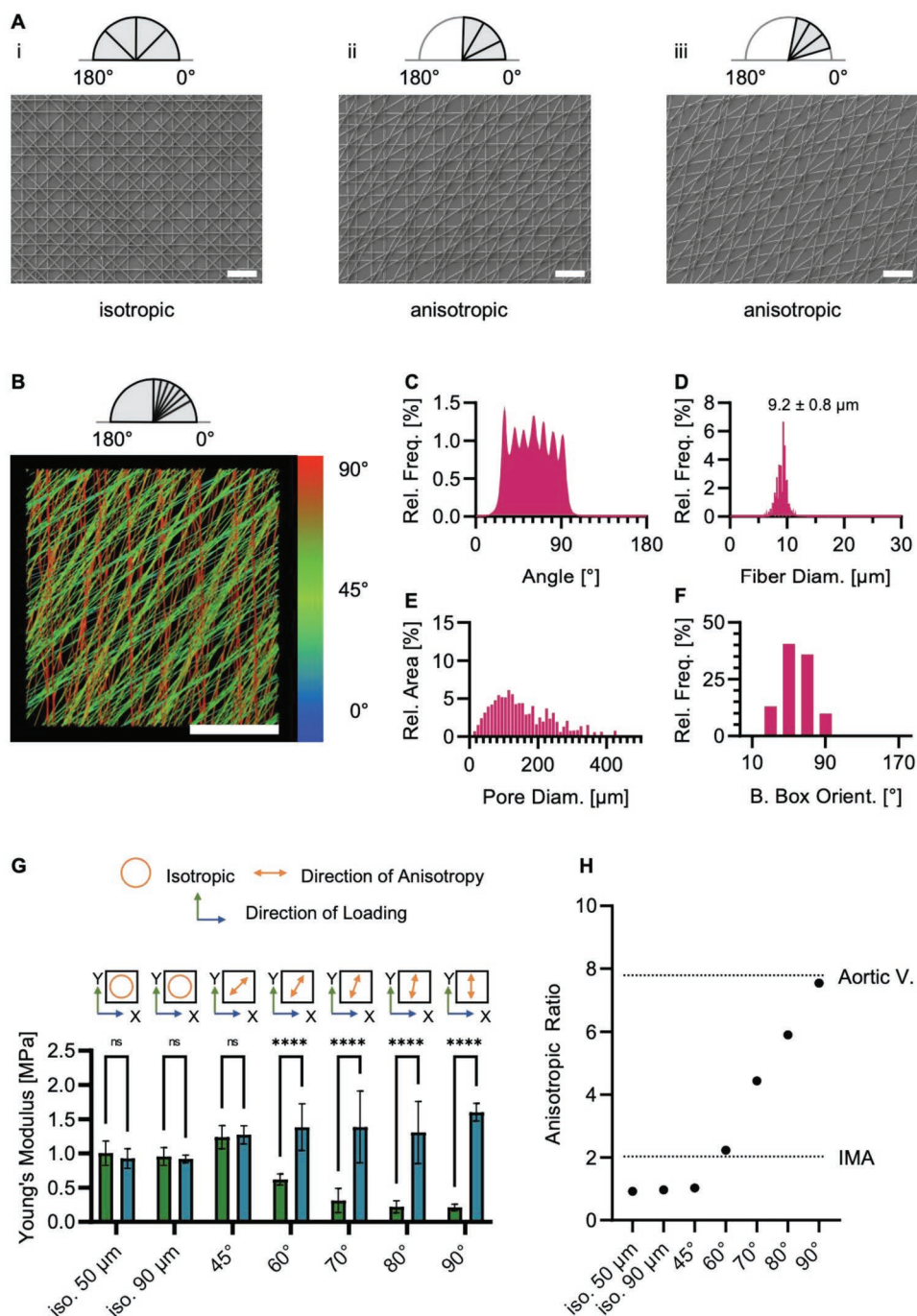


Figure 3. Restriction of the OV introduces anisotropy. A-i) Isotropic scaffolds result if the scaffold architecture is constructed from evenly distributed fiber orientations between 0° and 180°. ii) Anisotropy is introduced when the OV is restricted to entail only angles greater than 0° and/or smaller than 180°. iii) The closer OV_{min} and OV_{max} are, the more pronounced the anisotropy becomes (scale bars 200 μm). B) Color-coded reconstructed microCT data of an anisotropic architecture ($OV = [30^\circ, 40^\circ, \dots, 90^\circ]$, $ID = 250$ to 500 μm), with an average fiber direction of 60° fabricated via MEW in ten stacks (scale bar 1 mm). C) The resulting frequency distribution of fiber orientations peaks every 10° from 30° to 90°, as coded in the software platform to define the tool-paths for MEW with D) fiber diameter of 9.2 ± 0.8 μm. E) Resulting frequency distribution of pore diameters for the anisotropic scaffold, of which F) the pores were preferably oriented in 60° direction, as dictated by the coded architecture. G) The Young's Modulus strongly depends on the overall resulting fiber direction. H) The anisotropic ratio can be tailored to match human tissue such as the internal mammary artery (IMA)^[66] and the aortic valve.^[67]

now shows more elongated pores. It is important to note, that here the anisotropy arises from superimposed oriented fiber sets, which results in scaffolds with an interconnected fibrous

structure. This is in strong contrast to anisotropic scaffolds known from electrospinning, where a rotating drum is often used to collect aligned fibers.^[65] Such electrospun scaffolds

usually consist of mostly parallel fibers with little cohesion when loaded perpendicular to the fiber orientation and hence have limited usability.

Figure 3B shows the reconstructed microCT data of an anisotropic scaffold ($OV = [30^\circ, 40^\circ, \dots, 90^\circ]$, $ID = 250$ to $500 \mu\text{m}$, overall-resulting fiber direction of 60° , ten stacks), that has been analyzed with the same algorithms as the isotropic scaffolds. The color-coded scaffold, as well as the frequency distribution plot (Figure 3C) peaking in 10° steps from 30° to 90° confirm again the accurate translation of the coded scaffold architecture via MEW into an actual scaffold with a fiber diameter of $9.2 \pm 0.8 \mu\text{m}$ (Figure 3D). Here, we also found Gamma-distributed pores (Figure 3E and Table S1, Supporting Information) oriented in a preferred direction at 60° , as dictated by the coded fiber architecture which can be deduced from the orientation of the bounding boxes (Figure 3F).

To investigate the effects of the scaffold architecture on the mechanical properties, we performed tensile testing in two orthogonal directions (i.e. 0° and 90°) on scaffolds with different average fiber directions (Figure 3G). As expected, an isotropic design of the scaffolds showed non-significant differences in Young's modulus in the perpendicular loading directions. However, the differences per loading direction became strongly significant for scaffolds designed with average fiber directions of 60° , 70° , 80° , and 90° . Despite its anisotropic architecture, the 45° scaffold showed non-significant differences in the force responses, as its overall resulting fiber direction was symmetrically oriented between the directions of loading. The scaffold thickness had no effects on the stiffness (iso 50 vs iso 90 μm in Figure 3G), underlining, that it was the orientation of the fibrous microarchitecture that determined the mechanical response. The capacity of precisely depositing fibers enables the design of optimal load-bearing constructs. This has also been recently applied to scaffolds produced via fused filament fabrication (FFF) for bone tissue engineering by varying infill patterns, although still resulting in macro and channel-like pores.^[68–72] With our design approach, we could accurately tailor the anisotropic ratio from 1 (isotropic) to 7.5 (strongly anisotropic), which exemplary matches quite closely those of the left internal mammary artery,^[66] and of the human aortic valve tissue,^[67] respectively (Figure 3H).

Here, the scaffold's overall anisotropy arises from multiple layers of oriented fiber sets, which opens the possibility to design bioinspired constructs with precise control over their mechanical characteristics. The concept of superimposing layerwise anisotropic patterns results in an anisotropic structural component that is strongly bioinspired and can exemplary be found in the cellular alignment of the myocardium, which gradually transitions from a left-handed helix at the endocardium toward a right-handed helix at the epicardium.^[73]

Prospectively, stacks with different pore sizes and varying overall resulting fiber direction can be combined to form scaffolds with a structural and hence mechanical gradient along their thickness direction. Such a gradient would be desirable to, for example, mimic the gradient of the porous architecture from the cortical bone to the cancellous bone^[74] or to account for layer specific anisotropies as it is in the myocardium, corneal stroma, meniscus, or articular cartilage.^[73]

2.4. Microporosity Supports Cell Migration and Tissue Ingrowth

To study the suitability of the MEW scaffolds with controlled microporosity for cell migration and ingrowth, we seeded human umbilical artery smooth muscle cells (HUASMCs) on top of flat microporous scaffolds (with the design shown for scaffold 2 with eight stacks, thickness $300 \mu\text{m}$, Figure 4A). Cell infiltration was assessed after 3 and 7 days of culture. Cross-sectional cuts of scaffolds provide insight into the progressing cell proliferation and infiltration at the different time points (Figure 4B,C). After 3 days, single cells had bridged the pores inside the scaffolds by stretching between individual fibers (Figure 4B) and had reached the lower surface. Cell migration clearly progressed toward day 7 (Figure 4C), forming a covering cell layer on both sides of the scaffolds. We quantified the increasing cell number in the scaffold's cross section by deriving an area fraction of cellular components via image segmentation. In this way we found a significant increase in area fraction from $2.2 \pm 0.6 \%$ at day 3 to $10.9 \pm 2.2 \%$ at day 7 (Figure S6, Supporting Information). Successful cell infiltration was additionally highlighted by z-stacked fluorescence images (Figure 4B,C). Here, we found that the HUASMCs either bridged pores or oriented themselves along the fiber directions. As the z-stacked images cover a maximum depth of $75 \mu\text{m}$ the images at day 7 are dominated by the almost confluent cell layer on the upmost surface. Extracellular matrix production was visible at 28 days in the scaffold's micropores (Figure 4D).

This infiltration in 3D scaffolds is a different scenario to in vitro and in silico pore bridging experiments previously reported for rectangular MEW pores.^[75,76] These were performed for much larger channel-like pore sizes (200 – $600 \mu\text{m}$) of quasi 2D scaffolds, and identified that cells, in the first place, try to establish links between individual fibers before they start to actually fill the voids of a porous matrix.^[75]

Wissing et al. have pointed out the importance of scaffold microarchitecture (fiber diameter and fiber alignment) on the early macrophage-driven biomaterial degradation,^[77] where larger electrospun fiber diameter in the micrometer range^[78,79] and anisotropic patterns promoted the elongation of cells^[80] and polarized macrophages into the immunomodulatory and tissue remodeling (M2) phenotype.

In situ tissue engineering summons the regenerative potential of the human body to control cell functions for tissue repair, in the course of which, the implanted scaffold is degraded while being gradually replaced by autologous neo-tissue.^[6,8,81] This complex immunological response has to be carefully orchestrated to guide the tissue regeneration process from an early inflammatory phase to a proliferative phase that finally transitions in a remodeling phase.^[6] To start this cascade, efficient cell attachment and infiltration of the implanted acellular scaffold is key to the success of endogenous colonization by host cells.

By exploiting the capability of MEW to easily tune fiber diameter^[18] and combining it with our algorithm to control both pore size and morphology, our platform has the potential to realize, from an scaffold architectural point of view, the conditions to trigger and tune the immune response to have a positive impact on tissue regeneration in situ, although this remains to be verified. Other important aspects such as complex biochemical and biomechanical cues are also contributing to this.^[6,8,82]

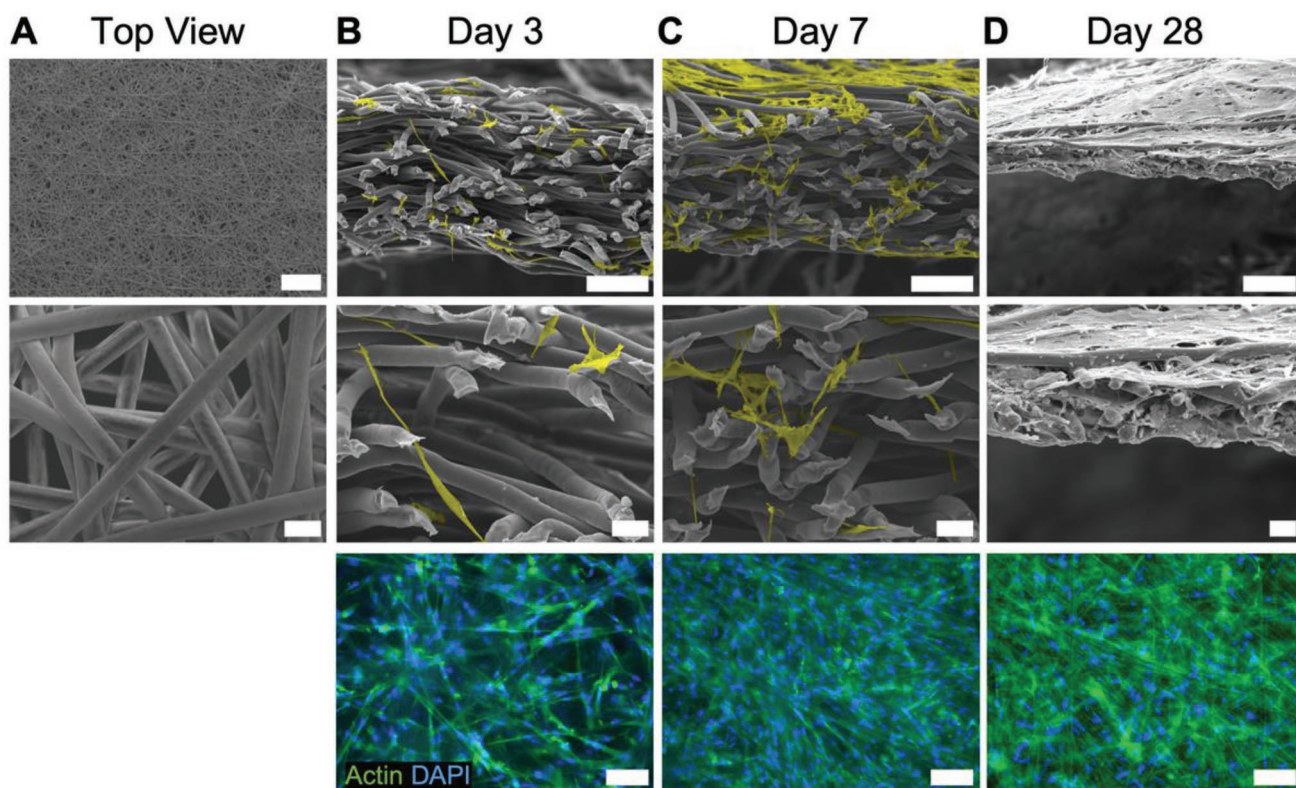


Figure 4. SEM and immunofluorescence evaluation of the scaffold infiltration by cells. A) Top view of the scaffold prior to seeding (scale bars 500 and 20 μm). B,C) SEM images of progressing migration of HUASMCs (colored in yellow) into the scaffold after 3 and 7 days (scale bars 100 and 20 μm). Top view z-stacked fluorescence images highlighting the formation of a dense cell population (scale bars 100 μm). D) SEM images of scaffold at 28 days showing extracellular matrix produced by the HUASMCs in the micropores (scale bars 100, 20, and 100 μm).

2.5. Microporous Tubular Scaffold Architectures

If a Gcode for a flat scaffold is printed on a tubular collector to form a cylindrical scaffold, an overlapping zone is needed to allow for closure of the tube along the axial direction.^[38] This overlapping zone, however, creates a structural and mechanical discontinuity that can result in unwanted stress distribution and failure. Thus, we expanded the proposed design strategy to output seamless tubular architectures (Figure 5A) (detailed in the Supporting Information). Here, we translated the possibility of designing both isotropic and anisotropic scaffolds by taking advantage of the “endless” circumferential axis when performing MEW on a tubular collector (Figure 5B,C). Exemplary, we demonstrate the fabrication of an isotropic tubular scaffold (OV [0°, 10°, ..., 170°], eight stacks) of 4 mm inner diameter with a wall thickness of 300 μm . The resulting scaffold architecture with continuous fibers can be appreciated from the microCT reconstructions shown in Figure 5D,E and Video S2, Supporting Information. Similarly to the flat architectures, the tubular designs enable the fabrication of constructs with multilayered alignment, as for example, known from the collagen fibers forming the annulus fibrosus of an intervertebral disk or the arrangement of smooth muscle and endothelial cells in blood vessels.^[73]

The capability to produce small diameter vascular grafts is demonstrated in Figure 5F,G showing a MEW tubular scaffold with 4 mm diameter and 300 μm wall thickness. We also

assessed the suture retention strength of tubular scaffolds (4 mm diameter) with 150 and 300 μm wall thickness. The 150 μm scaffold featured a 1.2 ± 0.2 N retention strength while the 300 μm scaffold reached a proportionally twofold higher at 2.6 ± 0.5 N (Figure 5H.) This range of forces well includes the characteristic suture retention of human internal mammary arteries (1.4 N) and human saphenous veins (1.8 N),^[83] which are the blood vessels of choice for coronary artery bypass grafting. Hence, we can conclude, that the suture retention strength can be tailored based on the number of stacks and thus the wall thickness. To showcase another perspective use case, we performed MEW of the isotropic pattern directly on a self-expanding 3 mm stent to obtain a covered stent with the MEW membrane bridging its macroscopic pores (Figure 5I,J).

3. Conclusion

In this work, we introduced a design concept to provide a platform for highly tunable microporous melt-electrowritten scaffolds. Our design approach allows to decouple fiber diameter and pore size to fabricate scaffolds characterized by pore morphologies and mechanical characteristics ranging from isotropic to highly anisotropic. The graphical user interface enables the easy design of scaffold architectures, whose response to tensile loading can be tailored to specifically match the anisotropy ratio of a wide range of human tissue

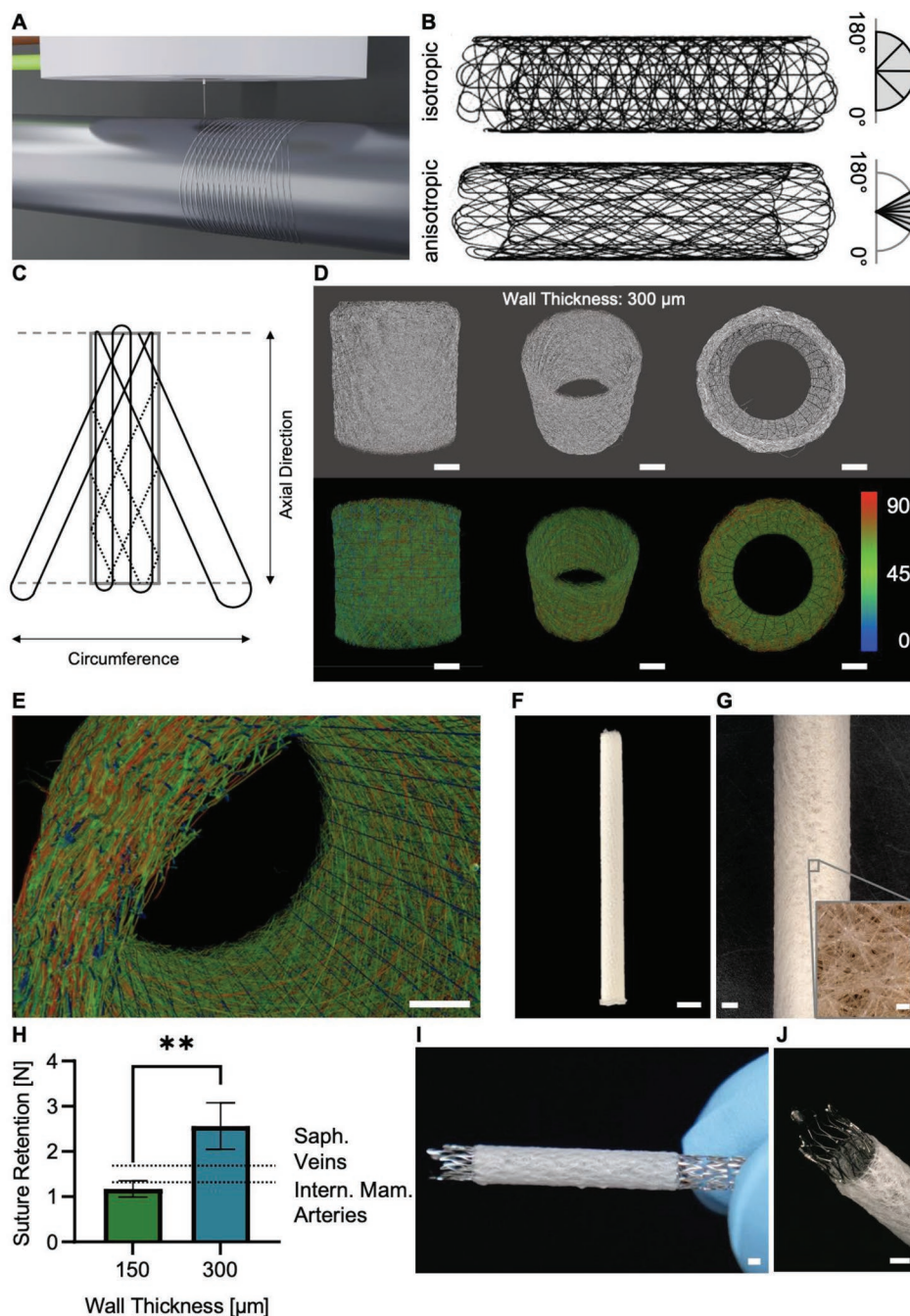


Figure 5. Translation of the design platform to seamless tubular architectures. A) Rendering of the continuous MEW fiber deposition during the fabrication of a tubular scaffold construct onto a rotating cylindrical collector. B) The software platform allows to design both isotropic and anisotropic tubular scaffold architectures by C) taking advantage of the endless circumferential axis of the rotating cylindrical collector. D) Reconstructed and color-coded microCT data of a tubular scaffold (\varnothing 4 mm, scale bars 1 mm) highlighting E) the microfibrous architecture in the tubular scaffold wall (scale bar 1 mm). F) Small diameter (\varnothing 4 mm, length 5 cm) vascular graft (scale bar 5 mm) with G) magnified view highlighting the microporous fiber architecture (scale bars 1 mm, 100 μ m). H) The suture retention of such tubular scaffolds can be tailored via the wall thickness to match the characteristics from human tissues, for example, the human saphenous veins and internal mammary arteries. Values of human tissue from König et al.^[83] I, J) Tubular scaffold architecture directly melt-electrowritten onto a 3 mm self-expanding stent (scale bars 1 mm).

types. Furthermore, the microporous architecture guided cellular attachment and subsequent ingrowth. Finally, this approach was expanded to enable the fabrication of seamless microporous tubular scaffolds via MEW. Hence, this software

platform for MEW provides a valuable tool for tissue engineers to fast and reproducibly fabricate highly controlled scaffold architecture with controlled microporosity in a plethora of embodiments.

4. Experimental Section

Software Platform: The software platform was developed in MATLAB R2020b (The Mathworks, USA). A Graphical User Interface translated user input data into Gcode commands readable for MEW setups. A detailed description of the algorithm is provided in the Supporting Information.

Melt Electrowriting: MEW was performed on a previously described setup.^[29] Medical grade poly(ϵ -caprolactone) (Purasorb PC12, Lot# 2004002576, Corbion, Netherlands) was heated at 75 °C in a 3 cc syringe (Nordson EFD, USA) and extruded through a 23 G needle (Nordson EFD, USA) heated to 85 °C. The needle protruded 1 mm out of the print head. If not stated otherwise, the polymer extrusion was guided by pressurized air (2 bar) applied to the syringe and a voltage of +4.5 kV applied to the needle at a working distance of 5 mm between the print head and a grounded metal collector. Flat scaffolds were printed onto 1 mm thick microscopy glass slides with a speed of 900 mm min⁻¹ (800 mm min⁻¹ for scaffolds shown in Figure 3H). Scaffolds shown in Figures 1B and 3A were printed with 0.5 bar and the scaffolds in Figures 2 and 3B with a pressure of 0.1 bar (Figure S1, Supporting Information, speed of 1600 mm min⁻¹), 0.5 bar (Figures S2 and S4, Supporting Information), and 2.0 bar (Figure S3, Supporting Information). Tubular scaffolds were directly melt-electrowritten (0.7 bar, 900 mm min⁻¹, 5 kV gradually increasing to 5.6 kV, 5 mm working distance increasing for 5 μ m per layer) onto a 4 mm diameter brass mandrel or a 3 mm diameter brass mandrel on which a sinus-superFlex-418 stent (optimized Medizinische Instrumente, Germany) was mounted.

Scaffold Architectures: The respective scaffold architectures are detailed in Table 1.

MicroCT: The microCT scans were performed on an Xradia 500 Versa (Zeiss, Germany) equipped with a 160 kV transmission tube and an indirect detection system made of a scintillator, switchable objective lenses (0.39 \times , 4 \times , 20 \times), and a CCD camera with 2048 \times 2048 pixels. The samples were either attached to a thin plastic plate before mounting (flat scaffolds) or placed directly on top of the sample holder (tubular scaffold).

The flat scaffolds were imaged at a source-to-sample distance of 20 mm and a sample-to-detector distance of 14 mm. The 4 \times objective

and a twofold detector binning (1024 \times 1024) were used for the acquisition, resulting in an effective pixel size of 4 μ m. The tomographic scans included 2401 radiographic projection images that were recorded over a sample rotation of 360° and with an exposure time of 2 s per image. The tube voltage and power were 80 kV and 6 W, respectively. Due to its small fiber diameter, scaffold 1 was additionally imaged with no detector binning (2048 \times 2048) to increase the spatial resolution to 2 μ m and better resolve the fibers. Here, 3201 images were recorded with an exposure time of 8 s. The scan parameters of the tubular scaffold were 60 kV tube voltage, 4 \times objective, no detector binning, 2.6 μ m pixel size, 2801 images, and 10 s exposure time.

Tomographic reconstruction of the acquired data and determination of the scaffolds' porosities was carried out with the software X-AID (MITOS, Germany). For an in-depth analysis of the pores each scaffold was sliced along the thickness direction in four planes, of which the data was projected into a 2D image accounting for equivalent layer numbers, that is, a single stack, per scaffold. From such a 2D image the orientation of the pores was extracted by fitting oriented bounding boxes around the pores using IPSDK Explorer 3.0.2.2 (Reactiv'IP, France). In addition, pixel counting was used to derive an area per pore, of which, assuming a circular pore shape, a pore diameter was deducted. Fiber orientation and fiber diameter assessment was performed with VG Studio Max 3.4.0 (Volume Graphics, Germany).

Tensile Testing and Suture Retention: Tensile testing ($n = 6$) was performed on a Zwickline Z2.5 (ZwickRoell, Germany) equipped with a 10 N load cell at a cross head speed of 60 mm min⁻¹. The stiffness was calculated in the linear section (0.1 to 0.4 N) of the force-strain curve by taking into account the scaffolds' thickness, measured with a digital precision indicator (ID-C1012B 543-270B, Mitutoyo, Germany). The suture retention ($n = 4$) was measured with the same setup at a cross head speed of 50 mm min⁻¹. One end of the tube was immobilized in the lower clamp, while the opposite end was pierced with a 7-0 suture (Covidien Surgipro II VP-704-MX, Medtronic, Ireland) \approx 2 mm inward. The suture was affixed to the moving cross head.

Cell Seeding on Scaffolds: For evaluating cell proliferation and infiltration on MEW scaffolds the selected construct architecture was that referred to as scaffold 2 in Figure 2. Before cell seeding, the scaffolds were cleaned using 70 % ethanol and then washed three

Table 1. Parameter overview of the scaffold architectures.

Scaffold type	#	Orientation vector [°]	Interfiber distance (ID_{min} – ID_{max}) [μ m]
Figure 1B	–	[0, 10, ..., 170] [0, 20, ..., 160] [0, 30, ..., 150] [0, 45, ..., 135]	67–133, 100–200, 150–300, 200–400, 250–500, 300–600
Figure 2	S1–S3	[0, 10, ..., 170]	250–500
Figure 3	A-i	[0, 45, ..., 135]	67–133
	A-ii	[0, 30, ..., 90]	67–133
	A-iii	[10, 33, ..., 90]	67–133
	B (S4)	[30, 40, ..., 90]	250–500
	iso. 50 μ m	[0, 15, ..., 165]	500
	iso. 90 μ m	[0, 30, ..., 150]	500
	45°	[0, 15, ..., 90]	500
	60°	[15, 30, ..., 105]	500
	70°	[25, 40, ..., 115]	500
	80°	[35, 50, ..., 120]	500
	90°	[45, 60, ..., 135]	500
Figure 4	S2	[0, 10, ..., 170]	250–500
Figure 5	tub	[0, 10, ..., 170]	250–500
Figure S3A	–	[0, 15, ..., 165]	250–500

times in phosphate-buffered saline (PBS, Sigma, Germany) to remove any chemical residues. HUASMCs (Promocell, Germany) were seeded directly onto 1 × 1 cm scaffold pieces clamped in 48-well CellCrown inserts (Merck, Germany). A total of 100 000 cells were resuspended in 100 µl of culture medium, pipetted directly onto the scaffold surface, and incubated for 1 h at 37 °C to allow for cell adhesion. After this time, additional 500 µl of medium were added to the wells. The culture medium used was Dulbecco's modified Eagle's medium (DMEM, Gibco, Germany) supplemented with 10 % fetal calf serum (FCS, Gibco, Germany), ascorbic acid (Sigma-Aldrich, Germany), and 1 % antibiotics/antimycotics (Gibco, Germany). The cell-seeded scaffolds were kept in a humid incubator at standard culture conditions (37 °C, 5 % CO₂) for up to 28 days, while the culture medium was renewed every 3 days.

Immunofluorescence: Samples were fixed for 1 h using methanol-free 4 % formaldehyde (Roth, Germany) in PBS followed by a washing step in PBS. Cell membranes were permeabilized using 0.1 % Triton-PBS for 1 h at room temperature. Samples were then incubated with 100 nm working solution of fluorescent phalloidin (Acti-Stain 488, Cytoskeleton, USA) for 1 h at 37 °C, followed by a washing step with PBS and nuclei counterstaining using DAPI (Carl Roth, Germany). Visualization was carried out using a fluorescence microscope (BZ-X800, Keyence, Germany).

SEM: Samples were fixed in 2 % glutaraldehyde in PHEM buffer for 10 min at room temperature, followed by washing steps in PHEM buffer. Samples were dehydrated in 30 %, 50 %, 70 %, and 90 % ethanol, and then three times in 100 % ethanol (Merck, Germany) for 10 min each. Chemical drying was performed on the samples using hexamethyldisilazane (HMDS, Sigma, Germany). After the drying procedure, the samples were sputtered coated with a 7 nm gold layer and visualized with a JSM-6390 (Jeol, Germany, accelerating voltage 10 kV). Fiber diameters ($n = 10$) in Figure 2 were measured with the SEM's built-in software. Cells in SEM images were colored in Mountains 9 (Digital Surf, France). Colorized images were color thresholded for yellow segments only using Fiji^[84] plugins in ImageJ.^[54] The segmented areas were used to quantify cell infiltration via an area fraction of cellular components in the SEM images ($n = 4$).

Statistical Analysis: Statistical analysis was performed with Prism 9.2.0 (GraphPad Software, USA). After confirmation of normal distribution ANOVA with *post hoc* Tukey multiple comparisons (fiber diameter), ANOVA with *post hoc* Šidák multiple comparisons (tensile testing), and an unpaired *t*-test (suture retention) were performed. Values are reported as mean ± standard deviation. ****: $p \leq 0.0001$, ***: $0.0001 < p \leq 0.001$, **: $0.001 < p \leq 0.01$, and *: $0.01 < p \leq 0.05$ were used to indicate the level of significance.

Supporting Information

Supporting Information is available from the Wiley Online Library or from the author.

Acknowledgements

The authors gratefully acknowledge the assistance of Dario Arcuti and Ilse Schunn in SEM imaging and the contribution of Paulina Kraus to Figure 5. This work was supported in part by Deutsche Forschungsgemeinschaft (DFG) Research Training Group under Grant GRK 2274, and DFG Grant 403170227 ArchiTissue.

Open access funding enabled and organized by Projekt DEAL.

Conflict of Interest

The authors declare no conflict of interest.

Data Availability Statement

The data that support the findings of this study are available from the corresponding author upon reasonable request.

Keywords

cell infiltration, mechanical anisotropy, melt electrowriting, pore morphology, pore size, randomized fibers, tissue engineering

Received: July 14, 2022

Revised: November 30, 2022

Published online: January 27, 2023

- [1] R. Langer, L. G. Cima, J. A. Tamada, E. Wintermantel, *Biomaterials* **1990**, *11*, 738.
- [2] L. G. Cima, J. P. Vacanti, C. Vacanti, D. Ingber, D. Mooney, R. Langer, *J. Biomech. Eng.* **1991**, *113*, 143.
- [3] R. Langer, J. P. Vacanti, *Science* **1993**, *260*, 920.
- [4] R. S. Langer, J. P. Vacanti, *Sci. Am.* **1999**, *280*, 86.
- [5] R. Langer, J. P. Vacanti, *Sci. Am.* **1995**, *273*, 130.
- [6] T. B. Wissing, V. Bonito, C. V. C. Bouten, A. I. P. M. Smits, *npj Regen. Med.* **2017**, *2*, 18.
- [7] D. Sengupta, S. D. Waldman, S. Li, *Ann. Biomed. Eng.* **2014**, *42*, 1537.
- [8] A. K. Gaharwar, I. Singh, A. Khademhosseini, *Nat. Rev. Mater.* **2020**, *5*, 686.
- [9] E. Mazza, A. E. Ehret, *J. Mech. Behav. Biomed. Mater.* **2015**, *48*, 100.
- [10] J. Kluin, H. Talacua, A. I. P. M. Smits, M. Y. Emmert, M. C. P. Brugmans, E. S. Fioretta, P. E. Dijkman, S. H. M. Söntjens, R. Duijvelshoff, S. Dekker, *Biomaterials* **2017**, *125*, 101.
- [11] P. X. Ma, R. Langer, in *Tissue Engineering Methods and Protocols*, Springer, New York **1999**, pp. 47–56.
- [12] M. Costantini, A. Barbetta, in *Functional 3D Tissue Engineering Scaffolds* (Eds: Y. Deng, J. Kuiper), Elsevier, New York **2018**, pp. 127–149.
- [13] H. Joukhdar, A. Seifert, T. Jüngst, J. Groll, M. S. Lord, J. Rnjak-Kovacina, *Adv. Mater.* **2021**, *33*, 2100091.
- [14] U. Boudriot, R. Dersch, A. Greiner, J. H. Wendorff, *Artif. Organs* **2006**, *30*, 785.
- [15] S. J. Eichhorn, W. W. Sampson, *J. R. Soc., Interface* **2005**, *2*, 309.
- [16] T. D. Brown, P. D. Dalton, D. W. Huttmacher, *Adv. Mater.* **2011**, *23*, 5651.
- [17] G. Hochleitner, T. Jüngst, T. D. Brown, K. Hahn, C. Moseke, F. Jakob, P. D. Dalton, J. Groll, *Biofabrication* **2015**, *7*, 035002.
- [18] A. Hrynevich, B. Ş. Elçi, J. N. Haigh, R. McMaster, A. Youssef, C. Blum, T. Blunk, G. Hochleitner, J. Groll, P. D. Dalton, *Small* **2018**, *14*, 1800232.
- [19] T. M. Robinson, D. W. Huttmacher, P. D. Dalton, *Adv. Funct. Mater.* **2019**, *29*, 1904664.
- [20] T. D. Brown, A. Slotosch, L. Thibaudeau, A. Taubenberger, D. Loessner, C. Vaquette, P. D. Dalton, D. W. Huttmacher, *Biointerphases* **2012**, *7*, 13.
- [21] E. McColl, J. Groll, T. Jüngst, P. D. Dalton, *Mater. Des.* **2018**, *155*, 46.
- [22] N. T. Saidy, T. Shabab, O. Bas, D. M. Rojas-Gonzalez, M. Menne, T. Henry, D. W. W. Huttmacher, P. Mela, E. M. De-Juan-Pardo, *Front. Bioeng. Biotechnol.* **2020**, *8*, 793.
- [23] P. D. Dalton, *Curr. Opin. Biomed. Eng.* **2017**, *2*, 49.
- [24] S. Bertlein, D. Hikimoto, G. Hochleitner, J. Hümmer, T. Jüngst, M. Matsusaki, M. Akashi, J. Groll, *Small* **2018**, *14*, 1701521.
- [25] A. Youssef, A. Hrynevich, L. Fladeland, A. Balles, J. Groll, P. D. Dalton, S. Zabler, *Tissue Eng., Part C* **2019**, *25*, 367.

- [26] M. Castilho, A. van Mil, M. Maher, C. H. G. Metz, G. Hochleitner, J. Groll, P. A. Doevendans, K. Ito, J. P. G. Sluijter, J. Malda, *Adv. Funct. Mater.* **2018**, *28*, 1803151.
- [27] K. M. A. Mueller, G. J. Topping, S. P. Schwaminger, Y. Zou, D. M. Rojas-González, E. M. De-Juan-Pardo, S. Berensmeier, F. Schilling, P. Mela, *Biomater. Sci.* **2021**, *9*, 4607.
- [28] O. Bas, D. D'Angella, J. G. Baldwin, N. J. Castro, F. M. Wunner, N. T. Saidy, S. Kollmannsberger, A. Reali, E. Rank, E. M. De-Juan-Pardo, *ACS Appl. Mater. Interfaces* **2017**, *9*, 29430.
- [29] N. T. Saidy, F. Wolf, O. Bas, H. Keijdener, D. W. Huttmacher, P. Mela, E. M. De-Juan-Pardo, *Small* **2019**, *15*, 1900873.
- [30] N. C. Paxton, R. Daley, D. P. Forrestal, M. C. Allenby, M. A. Woodruff, *Mater. Des.* **2020**, *193*, 108787.
- [31] J. Kim, E. Bakirci, K. L. O'Neill, A. Hrynevich, P. D. Dalton, *Macromol. Mater. Eng.* **2021**, *306*, 2000685.
- [32] F. Tourlomousis, H. Ding, D. M. Kalyon, R. C. Chang, *J. Manuf. Sci. Eng.* **2017**, *139*, 081004.
- [33] H. Ding, K. Cao, F. Zhang, W. Boettcher, R. C. Chang, *Mater. Des.* **2019**, *178*, 107857.
- [34] Y. Zhang, A. L. Fricc, M. Chen, *Int. J. Pharm.* **2021**, *606*, 120841.
- [35] T. Jungst, I. Pennings, M. Schmitz, A. J. W. P. Rosenberg, J. Groll, D. Gawlitta, *Adv. Funct. Mater.* **2019**, *29*, 1905987.
- [36] I. Pennings, E. E. van Haaften, T. Jungst, J. A. Bulsink, A. J. W. P. Rosenberg, J. Groll, C. V. C. Bouten, N. A. Kurniawan, A. I. P. M. Smits, D. Gawlitta, *Biofabrication* **2019**, *12*, 015009.
- [37] C. Großhaus, E. Bakirci, A. Hrynevich, J. C. Kade, G. Hochleitner, J. Groll, P. D. Dalton, *Small* **2020**, *16*, 2003471.
- [38] N. T. Saidy, A. Fernández-Colino, B. S. Heidari, R. Kent, M. Vernon, O. Bas, S. Mulderrig, A. Lubig, J. C. Rodríguez-Cabello, B. Doyle, D. W. Huttmacher, E. M. De-Juan-Pardo, P. Mela, *Adv. Funct. Mater.* **2022**, *32*, 2110716.
- [39] M. Stasiak, A. Studer, A. Greiner, J. H. Wendorff, *Chem. - Eur. J.* **2007**, *13*, 6150.
- [40] S. Ramakrishna, K. Fujihara, W.-E. Teo, T. Yong, Z. Ma, R. Ramaseshan, *Mater. Today* **2006**, *9*, 40.
- [41] C. Kim, K. S. Yang, M. Kojima, K. Yoshida, Y. J. Kim, Y. A. Kim, M. Endo, *Adv. Funct. Mater.* **2006**, *16*, 2393.
- [42] S. J. Grainger, A. J. Putnam, *PLoS One* **2011**, *6*, e22086.
- [43] L. L. Y. Chiu, M. Radisic, *Biomaterials* **2010**, *31*, 226.
- [44] F. M. Wunner, M. Wille, T. G. Noonan, O. Bas, P. D. Dalton, E. M. De-Juan-Pardo, D. W. Huttmacher, *Adv. Mater.* **2018**, *30*, 1706570.
- [45] J. He, G. Hao, Z. Meng, Y. Cao, D. Li, *Adv. Mater. Technol.* **2021**, *7*, 2101197.
- [46] S. H. Oh, I. K. Park, J. M. Kim, J. H. Lee, *Biomaterials* **2007**, *28*, 1664.
- [47] I. Bružauskaitė, D. Bironaitė, E. Bagdonas, E. Bernotienė, *Cytotechnology* **2016**, *68*, 355.
- [48] Y. Han, M. Lian, Q. Wu, Z. Qiao, B. Sun, K. Dai, *Front. Bioeng. Biotechnol.* **2021**, *9*, 495.
- [49] A. Balguid, A. Mol, M. H. van Marion, R. A. Bank, C. V. C. Bouten, F. P. T. Baaijens, *Tissue Eng., Part A* **2009**, *15*, 437.
- [50] G. Hochleitner, A. Youssef, A. Hrynevich, J. N. Haigh, T. Jungst, J. Groll, P. D. Dalton, *BioNanomaterials* **2016**, *17*, 159.
- [51] S. Zhong, Y. Zhang, C. T. Lim, *Tissue Eng., Part B* **2012**, *18*, 77.
- [52] A. D'Amore, J. A. Stella, W. R. Wagner, M. S. Sacks, *Biomaterials* **2010**, *31*, 5345.
- [53] N. A. Hotaling, K. Bharti, H. Kriel, C. G. Simonjr, *Biomaterials* **2015**, *61*, 327.
- [54] C. A. Schneider, W. S. Rasband, K. W. Eliceiri, *Nat. Methods* **2012**, *9*, 671.
- [55] K.-W. Lee, D. B. Stolz, Y. Wang, *Proc. Natl. Acad. Sci. USA* **2011**, *108*, 2705.
- [56] A. Fernández-Colino, F. Wolf, H. Keijdener, S. Rütten, T. Schmitz-Rode, S. Jockenhoewel, J. C. Rodríguez-Cabello, P. Mela, *Mater. Sci. Eng. C* **2018**, *88*, 140.
- [57] G. Hochleitner, J. F. Hümmer, R. Luxenhofer, J. Groll, *Polymer* **2014**, *55*, 5017.
- [58] G. Hochleitner, F. Chen, C. Blum, P. D. Dalton, B. Amsden, J. Groll, *Acta Biomater.* **2018**, *72*, 110.
- [59] M. Gwiazda, S. Kumar, W. Świeszkowski, S. Ivanovski, C. Vaquette, *J. Mech. Behav. Biomed. Mater.* **2020**, *104*, 103631.
- [60] K. M. Kennedy, A. Bhaw-Luximon, D. Jhurry, *Acta Biomater.* **2017**, *50*, 41.
- [61] J. L. Lowery, N. Datta, G. C. Rutledge, *Biomaterials* **2010**, *31*, 491.
- [62] P. R. Johnston, *J. Test. Eval.* **1983**, *11*, 117.
- [63] P. R. Johnston, *Filtr. Sep.* **1998**, *35*, 287.
- [64] C. T. J. Dodson, W. W. Sampson, *J. Pulp Pap. Sci.* **1996**, *22*, J165.
- [65] B. Sun, X.-J. Jiang, S. Zhang, J.-C. Zhang, Y.-F. Li, Q.-Z. You, Y.-Z. Long, *J. Mater. Chem. B* **2015**, *3*, 5389.
- [66] M. Stekelenburg, M. C. M. Rutten, L. H. E. H. Snoeckx, F. P. T. Baaijens, *Tissue Eng., Part A* **2009**, *15*, 1081.
- [67] A. Balguid, M. P. Rubbens, A. Mol, R. A. Bank, A. J. J. C. Bogers, J. P. Van Kats, B. A. J. M. De Mol, F. P. T. Baaijens, C. V. C. Bouten, *Tissue Eng.* **2007**, *13*, 1501.
- [68] A. Gleadall, D. Visscher, J. Yang, D. Thomas, J. Segal, *Burns Trauma* **2018**, *6*, 19.
- [69] R. Baptista, M. Guedes, *J. Mech. Behav. Biomed. Mater.* **2021**, *117*, 104378.
- [70] K. Wang, X. Xie, J. Wang, A. Zhao, Y. Peng, Y. Rao, *Results Phys.* **2020**, *18*, 103346.
- [71] A. A. Ansari, A. Golebiowska, M. Dash, P. Kumar, P. K. Jain, S. Nukavarapu, S. Ramakrishna, H. S. Nanda, *Biomater. Sci.* **2022**, *10*, 2789.
- [72] X. Li, L. Wang, Y. Fan, Q. Feng, F. Cui, F. Watari, *J. Biomed. Mater. Res., Part A* **2013**, *101*, 2424.
- [73] J. Xing, N. Liu, N. Xu, W. Chen, D. Xing, *Adv. Funct. Mater.* **2021**, *32*, 2110676.
- [74] N. Abbasi, A. Abdal-Hay, S. Hamlet, E. Graham, S. Ivanovski, *ACS Biomater. Sci. Eng.* **2019**, *5*, 3448.
- [75] M. Lanaro, M. P. McLaughlin, M. J. Simpson, P. R. Buenzli, C. S. Wong, M. C. Allenby, M. A. Woodruff, *Acta Biomater.* **2021**, *136*, 429.
- [76] A. P. Browning, O. J. Maclaren, P. R. Buenzli, M. Lanaro, M. C. Allenby, M. A. Woodruff, M. J. Simpson, *J. Theor. Biol.* **2021**, *528*, 110852.
- [77] T. B. Wissing, V. Bonito, E. E. van Haaften, M. van Doeselaar, M. M. C. P. Brugmans, H. M. Janssen, C. V. C. Bouten, A. I. P. M. Smits, *Front. Bioeng. Biotechnol.* **2019**, *7*, 87.
- [78] K. Garg, N. A. Pullen, C. A. Oskeritzian, J. J. Ryan, G. L. Bowlin, *Biomaterials* **2013**, *34*, 4439.
- [79] Z. Wang, Y. Cui, J. Wang, X. Yang, Y. Wu, K. Wang, X. Gao, D. Li, Y. Li, X.-L. Zheng, *Biomaterials* **2014**, *35*, 5700.
- [80] F. Y. McWhorter, T. Wang, P. Nguyen, T. Chung, W. F. Liu, *Proc. Natl. Acad. Sci. U. S. A.* **2013**, *110*, 17253.
- [81] B. J. de Kort, S. E. Koch, T. B. Wissing, M. M. Krebber, C. V. C. Bouten, A. Smits, *Adv. Drug Delivery Rev.* **2021**, *178*, 113960.
- [82] S. Camarero-Espinosa, M. C. Oliveira, H. Liu, J. F. Mano, N. Bouvy, L. Moroni, *Adv. Healthcare Mater.* **2021**, *11*, 2101415.
- [83] G. Konig, T. N. McAllister, N. Dusserre, S. A. Garrido, C. Iyican, A. Marini, A. Fiorillo, H. Avila, W. Wystrychowski, K. Zagalski, M. Maruszewski, A. L. Jones, L. Cierpka, L. M. de la Fuente, N. L'Heureux, *Biomaterials* **2009**, *30*, 1542.
- [84] J. Schindelin, I. Arganda-Carreras, E. Frise, V. Kaynig, M. Longair, T. Pietzsch, S. Preibisch, C. Rueden, S. Saalfeld, B. Schmid, *Nat. Methods* **2012**, *9*, 676.